A Non-Contact Vital Signs Detection in a Multi-Channel 77GHz LFMCW Radar System

QISONG WU [ID]1, (Member, IEEE), ZENGYANG MEI [ID]1,
ZHICHAO LAI [ID]1, (Graduate Student Member, IEEE),
DIANZE LI1, (Graduate Student Member, IEEE), AND DIXIAN ZHAO [ID]2
[1]Key Laboratory of Underwater Acoustic Signal Processing of Ministry of Education, Southeast University, Nanjing 210096, China
[2]National Mobile Communications Research Laboratory, Southeast University, Nanjing 210096, China

Corresponding author: Qisong Wu (qisong.wu@seu.edu.cn)

ABSTRACT The technology of vital signs detection has been proven of great use, whereas it is still limited by several challenges. One of the major challenges is the random body movements (RBMs), which significantly degrade the accuracy of the measurement. In this paper, a multi-channel 77GHz linear frequency modulated continuous-wave (LFMCW) radar system is investigated to perform vital signs monitoring on multiple targets with the mitigation of RBMs and a novel vital signs detection scheme is provided for the accurate estimates of the respiration rate (RR) and heart rate (HR). In the proposed scheme, a multi-channel Kalman smoother is firstly proposed to address the outliers in the extracted phase histories from the echoes in the multiple receivers, so that enhanced outlier-robust phase histories are acquired for the subsequent estimates of the RR and HR. Furthermore, a novel regional hidden Markov model is then proposed to carry out accurate estimates of RR and HR by exploiting the underlying slowly-varying characteristics of these vital signs for further mitigation of the effects of RBMs. Experimental results demonstrate that the estimated errors in the proposed scheme are less than 2 beats per minute (bpm) for both RR and HR under normal scenarios with young men in the RBMs environment.

INDEX TERMS Non-contact vital signs detection, linear-frequency-modulated continuous-wave (LFMCW) radar, random body movement (RBM), multi-channel Kalman smoother, hidden Markov model.

I. INTRODUCTION

Non-contact vital signs detection is of great significance to biomedical treatments, health monitoring and disaster tracing [1]–[4]. Over the last two decades, a huge amount of efforts have been devoted to non-contact vital signs detection researches to improve the accuracy [5]–[12]. The most fundamental is continuous-wave (CW) radar which uses a single frequency to detect the phase shift caused by chest displacement. However, it is difficult for CW radar to distinguish multiple targets on account of its lack of range resolution. To address this issue, the linear frequency-modulated continuous-wave (LFMCW) radar is considered and applied

to this field [13], [14], making it possible to detect multiple targets simultaneously.

Non-contact vital signs detection is based on sensing tiny physiological movements of several millimeters to several centimeters. However, random body movement (RBM), which has a displacement comparable to or larger than the chest wall displacement caused by vital signs, is a substantial noise source that can destroy the signals of interest, and thus drastically decay the estimated accuracy of vital signs. The basic function of vital sign detection requires the detection device to extract the low-frequency displacement information caused by these physiological movements from a high-frequency phase-modulated carrier signal, whereas the large-scale RBM relative to the tiny displacement from vital signs would disrupt the purity of the vital sign information.

The associate editor coordinating the review of this manuscript and approving it for publication was Hasan S. Mir.

This displacement from the large-scale RBM would deviate from the normal one from the vital signs of interest and can be regarded as an abnormality.

A number of efforts have been devoted to address the difficulty of RBM [10], [15]–[21]. Two doppler radar systems were considered and used to perform the RBM cancellation based on different body orientations [10], [15]. The self and mutual injection-locking technique were applied to cancel RBM with two radar systems [16]. The characteristic of the frequency spectrum of the vital signs signal under 1-D body motion was analyzed, motion direction detection and the respiration rate (RR) measurement under 1-D body motion were estimated using a CW Doppler radar [17]. Matched filter (MF) techniques were applied to measure the RR and heart rate (HR) in the large-scale RBM [18]. A moving average filter combined with a threshold method was applied to remove the interference [19], and an auto-correlation based technique was proposed in [20]. In [21], the vital signs signal was divided into segments and constructed based on the correlation concept.

To cope with the RBM challenge, we propose a novel vital signs detection scheme for the accurate estimates of both RR and HR. In the paper, a 77GHz LFMCW radar system with multiple receiver channels is firstly investigated to mitigate the interferences from multiple targets, and then a multi-channel Kalman smoother (MCKS) is proposed to acquire enhanced outlier-robust phase histories for the subsequent estimates of RR and HR. Furthermore, a novel regional hidden Markov model (RHMM) is finally proposed to carry out accurate estimates of RR and HR by exploiting the underlying slowly-varying characteristics of these vital signs for further mitigation of RBMs. Unlike the traditional hidden Markov model (HMM) with the tiresome computation burden, the proposed RHMM, which takes full advantage of the effective frequency ranges of RR and HR, has the capacity of realizing the fast acquisition of vital signs. Experiments demonstrate that the proposed MCKS method has the obvious gain increases of local signal to noise ratios (LSNRs) in RR and HR over those in the state-of-the-art methods, and the estimated errors of the proposed method are less than 2 beats per minute (bpm) for both RR and HR under normal scenarios with two young men in the RBMs environment.

This paper is organized as follows. Section II introduces the basic theory of LFMCW radar and vital signs signal. In Section III, the algorithms of the proposed MCKS and RHMM are presented. Section IV shows simulations results. Experimental results are provided and compared in Section V. Discussion is given in Section VI. Finally, a conclusion is drawn in Section VII.

Notation: We use lower-case (upper-case) bold characters to denote vectors (matrices). $\mathcal{N}(x|a, b)$ denotes that real-value random variable x follows a Gaussian distribution with mean a and variance b, and round(x) rounds each element of x to the nearest integer. $X \in \mathcal{R}^{N \times M}$ and $X \in \mathcal{C}^{N \times M}$ denote real-value and complex-value matrixes X with the dimensions of $N \times M$. $(\cdot)^*$ denotes the conjugate operation,

and sinc$(x) = \sin(\pi x)/(\pi x)$. Gamma$(\cdot)$ represents a Gamma distribution, and diag(x) represents a diagonal matrix that uses the elements of x as its diagonal elements. $\langle x \rangle$ denotes the expectation operator of the random variable x, and $\lfloor x \rfloor$ rounds the elements of x to the nearest integers towards infinity.

II. THEORY

A. PHASE EXTRACTION BASED ON LFMCW RADAR

Periodic linearly-increasing frequency chirps are commonly used as a transmission signal waveform for the LFMCW radar. The transmitted pulsed signal can be written as [13],

$$s_{\text{TX}}(t) = \sigma_{\text{TX}} \exp\left(j2\pi f_c t + j\pi \gamma t^2\right), \quad (1)$$

where σ_{TX} denotes the amplitude of signal, and f_c is the carrier frequency. $t \in (0, T)$ is the fast time with the sweep time of T and γ is the chirp rate, and thus the transmitted bandwidth is $B = \gamma T$. Assume M targets in the observed scenario and the distance from the radar to the mth target is $R_m(\tau)$ with the so-called 'slow time' τ. The received echo is given by

$$s_{\text{RX}}(t) = \sum_{m=1}^{M} \rho_m s_{\text{TX}}(t - \frac{2R_m(\tau)}{c}), \quad (2)$$

where ρ_m is the scatter coefficient of the mth target and c is the electromagnetic wave propagation speed. It should be noted that the distance $R_m(\tau)$ involves the initial range R_{m0} of the mth target and its tiny displacements of the chest wall in the vital signs detection. The beat signal can be obtained by mixing the received signal with the transmitted signal, and be written as

$$\begin{aligned} s_b(t) &= s_{\text{TX}}(t)s_{\text{RX}}^*(t) \\ &= \sum_{m=1}^{M} \sigma_{\text{TX}}\rho_m \exp\left(j\left(\frac{4\pi \gamma R_m(\tau)}{c}t + \frac{4\pi}{\lambda}R_m(\tau)\right)\right). \end{aligned} \quad (3)$$

The residual video phase, which is a quadratic term of τ, is found to be negligible and can then be ignored due to relatively small τ [22].

According to Eq.(3), the beat signal exhibits a constant frequency, which is proportional to the target range. This means that the distance information is contained in the frequency domain. We perform a fast Fourier transform (FFT) over the beat signal, and acquire its associated range profile as,

$$S_b(f) = \sum_{m=1}^{M} \sigma_{\text{TX}}\rho_m T \exp\left(j4\pi R_m(\tau)/\lambda\right)$$
$$\times \text{sinc}\left(T\left(f - 2\gamma R_m(\tau)/c\right)\right). \quad (4)$$

Considering the fact that the LFMCW radar system is able to differentiate the multiple targets in range due to the transmitted bandwidth B, and we have the range resolution as,

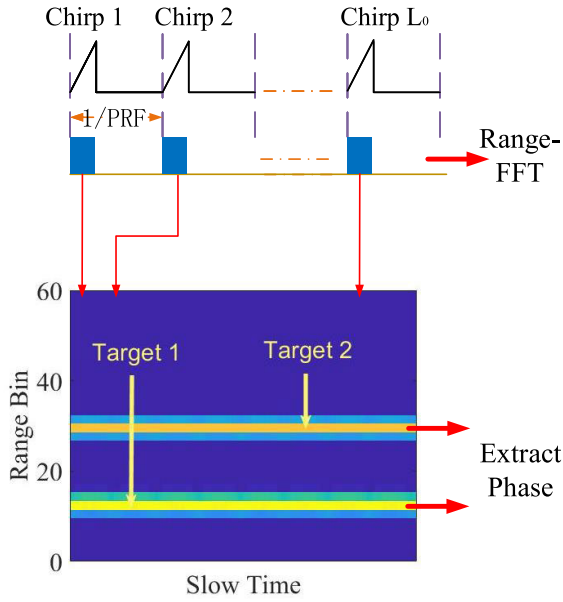$$\Delta R = \frac{c}{2B} \quad (5)$$

FIGURE 1. Range profile acquisition in the LFMCW radar system.

Fig.1 shows the range profile acquisition in the LFMCW radar system, where PRF denotes the pulse repetition frequency and can be given by $f_{PRF} = 1/T$. The constant false alarm rate (CFAR) technique is often used for the target detection [23], and the corresponding range bins can be acquired. To be specific, the CFAR detection result of one target is often spread in multiple continuous range bins instead of a single bin due to the limited bandwidth. The stripe with the strongest energy is just the range bin where the target is located. Furthermore, the phase histories in the detected range bins can be extracted for the subsequent vital signs detection. It is clear that the vital signs of multiple targets can be detected simultaneously with the LFMCW radar system.

For a LFMCW radar intended to monitor vital signs, a close look must be given at the exponential factor in Eq.(4). The desired phase history $\phi_m(\tau)$ of the *m*th target is related to the range evolution of target $R_m(\tau)$,

$$\phi_m(\tau) = \frac{4\pi R_m(\tau)}{\lambda}, \qquad (6)$$

where $m \in \{1, \ldots, M\}$. Multiple phase histories can be extracted for the estimates of HR and RR in multiple-target environment.

In the vital signs monitoring, the target's range evolution is mainly reflected in the displacements of the chest wall. These displacements are normally of small scale and the vital signs are quite weak. According to Eq.(6), it is found that a smaller wavelength λ will give a better displacement sensitivity. For example, if a displacement in the range is as small as 1 mm and λ is 4 mm, the corresponding fluctuation in phase history is $\Delta\phi_m = \pi$. In our work, a 77GHz radar

system is examined and investigated for this tiny physiological movement monitoring.

Note that a tiny displacement could bring a relatively large fluctuation in the phase term, the phases are seriously 'wrapped' in practice due to the chest displacement which can be even up to 12 mm in the normal scenarios. This phenomenon would get worse in the RBM environment with even up to 10 cm displacement. Normally, in a free-RBM scenario, the unwrapped phase histories are generally smooth due to the slowing-varying characteristic of RR and HR. However, the unwrapped phase histories would have considerable fluctuations which can even be up to dozens of radians in the RBMs scenario. To cope with this issue, a phase unwrapping process is often requisite, and then the unwrapped phase histories from multiple channels will be used for the subsequent processing.

B. VITAL SIGNS SIGNAL MODEL

Vital signs signal is originated from the periodic motion which is caused by respiration and heartbeat together. The magnitude and frequency of these two motion signals are regulated by the nerve center of human brain and are independent of each other. Generally, these two motion signals often have harmonic and intermodulation effects during the receiving process. Each motion signal is often approximated as the superposition of sinusoidal signals, and vital signs signal can be expressed as [8]

$$r(\tau) = \sum_i A_{ri}(\tau) \cos(2\pi i f_r(\tau)\tau) + A_h(\tau) \cos(2\pi f_h(\tau)\tau),$$

$$(7)$$

where $A_{ri}(\tau)$ is the amplitude of the *i*th harmonic of respiration and $A_h(\tau)$ is the amplitude of heartbeat signal at time τ. $f_r(\tau)$ and $f_h(\tau)$ respectively denote the RR and HR at time τ, which slowly change over time in essence. This underlying characteristic will be used to enhance the accuracies of vital signs detection in the RBM environment. The effect of harmonic of heartbeat can often be neglected owing to the its slight amplitude and relatively large frequency [8], shown in Eq. (7). In general, the amplitude range of A_{ri} in respiration is about [0.1, 12] mm, and the corresponding frequency of f_r often lies in [0.1, 0.5] Hz, whereas the amplitude range of A_h is about [0.01, 0.5] mm, and the frequency f_h often lies in [0.8, 3.0] Hz.

Considering the fact that such tiny displacements $r(\tau)$ are much smaller than the range resolution (The bandwidth of 2 GHz responses to the resolution of 7.5 cm), the range evolution contributed from the physiological movement generally fails to cross the range gate, as shown in Fig. 1. It is clear that they are located in the same range bins across L_0 chirps, respectively.

Suppose that the initial distance from the *m*th target to the radar system is R_{m0} and the corresponding vital signs displacement is $r_m(\tau)$. Looking close back to Eq.(6), the range

evolution of this target $R_m(\tau)$ can be written as

$$R_m(\tau) = R_{m0} - r_m(\tau). \qquad (8)$$

It is observed that the R_{m0} is almost a constant during the limited observed chirps. It would result in a strong direct-current (DC) component in the spectrum, and deteriorate the estimates of RR and HR. A notch filter would be introduced to address this issue. The negative symbol in Eq. (8) denotes the displacement of wall chest towards the radar.

C. MULTI-CHANNEL VITAL SIGNS SIGNALS

A radar system with multiple receivers has the capability of distinguishing multiple targets with diverse bearings and can be often used for bearing estimation. On the other hand, multiple receivers are also used to improve the SNR of signals of interest. In this paper, we take the latter into consideration for accurate vital signs estimation.
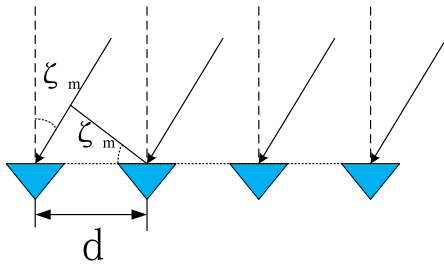

FIGURE 2. The schematic diagram of multiple receivers.

Assume the bearing of the mth target is denoted by ζ_m, shown in Fig.2, we acquire the difference of phase histories between the reference (assume the first receiver channel is referred as the reference one) and the pth channel as,

$$\Delta\phi_{m,p} = \frac{2\pi(p-1)d\sin\zeta_m}{\lambda}, \qquad (9)$$

where $p = 1, \ldots P$ and d denotes the element interval (P is the total number of elements and $P = 4$ in our radar system). It should be pointed out that $\Delta\phi_{p,m}$ is constant across chirps, and thus it can be regarded as a DC component. Therefore, we have the phase history in the pth receivers as,

$$\phi_{m,p}(\tau) = \Delta\phi_{m,p} + \phi_m(\tau). \qquad (10)$$

Note that $\phi_m(\tau)$ is a common component across channels, and contains the related vital signs information. However, $\Delta\phi_{m,p}$ is independent on the slow time τ, and is a constant value given a certain channel. The property above will be taken into consideration for the improved estimates of vital signs in the following section.

D. RANDOM BODY MOVEMENTS MODEL

Fig.3 illustrates the RMBs signal model. The target naturally moves his body and then returns to the original position,
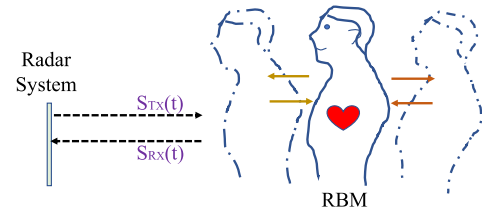

FIGURE 3. The illustration of the RBMs model.

therefore, the corresponding signal of one RBM period is often modeled as a series of triangular pulses in time domain with various amplitudes and durations, and can be expressed as [18],

$$b(\tau)$$
$$= \begin{cases} A_1 - A_1 \times 2|\tau - T_1/2|/T_1, & 0 \le \tau < T_1, \\ A_2 - A_2 \times 2|\tau - T_2/2 - T_1|/T_2, & T_1 \le \tau < T_1 + T_2, \\ \ldots & \ldots \\ A_n - A_n & T_1 + \ldots + T_{n-1} \le \tau \\ \times 2|\tau - T_n/2 - T_1 - \cdots - T_{n-1}|, & < T_1 + \cdots + T_n, \\ 0, & \text{others}, \end{cases}$$
$$(11)$$

where $A_1, A_2, \ldots, A_n$ are the amplitudes of n different triangular pulses, and $T_1, T_2, \ldots, T_n$ denote their durations respectively. The sign of the amplitude is negative if the RBM direction is toward the radar system, and when the RBM direction is backward, the sign is positive. It is found that both this RBMs signal $b(\tau)$ and vital sign signal $r_m(\tau)$ will be involved in the range evolution $R_m(\tau)$ of the mth target, and they will be considered in the subsequent vital signs detection.

It is observed that the spectrum of the RBMs signal is typically wide-band, and its low-frequency component is dominant. It would lead to coincide with the frequency ranges of RR and HR. It is a reason why the RBMs would deteriorate the estimated accuracies of RR and HR.

III. METHODOLOGY
A. MULTI-CHANNEL ROBUST KALMAN SMOOTHER

Considering the fact that the $\Delta\phi_{m,p}$ is constant and independent of τ, we apply a notch filter to remove these phase differences across channels and acquire the common term $\phi_m(\tau)$ associated with the physiological movement. Herein, a notch filter with the DC suppression is employed on the unwrapped phase histories of the multiple channels respectively to remove the phase differences and eliminate the components caused by the channel locations. The transfer function $H(z)$ of the filter is given by [24]

$$H(z) = \frac{1 + \alpha z^{-1} + z^{-2}}{1 + \alpha\mu z^{-1} + \mu^2 z^{-2}}, \qquad (12)$$
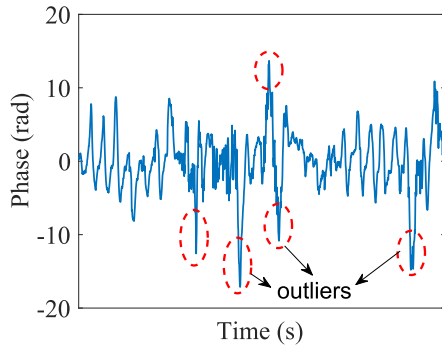
FIGURE 4. Unwrapped phase history after notch filter in the RBMs case.

where α is related with the notch frequency, and μ is related with the notch bandwidth. These parameters are given by [24],

$$\alpha = -2\cos\omega_0, \tag{13}$$

$$\mu^2 = \frac{1 - \tan(B_n/2)}{1 + \tan(B_n/2)}, \quad \mu > 0, \tag{14}$$

where ω_0 is the notch frequency, and B_n denotes the notch bandwidth. Note that notch filter width should be carefully considered. A wide notch width will degrade the SNR of RR due to its relatively low-frequency range of [0.1, 0.5] Hz, whereas too narrow width is not a good choice, because $\Delta\phi_{m,p}$ is not absolutely constant across chirps in a real radar system. With respect to the DC component, the value of ω_0 often approaches zero. One common and effective way to alleviate the noise fluctuations is to average phase histories after the notch filter [25]. However, it is known to us that the multi-channel average (MCA) operator is sensitive to the outliers, which often occur in large-scale RBM environments. Therefore, the average operator is not an optimal way to estimate the phase histories in the multiple channels, particularly in the RBM case. Fig. 4 shows a typical example of the unwrapped phase data after performing the notch filter in the RBM condition in the experiment. It is observed that the parts of the extracted phase history during the RBM period would deviate from the normal one, and have a few abnormal values.

To cope with these outliers caused by RBMs, a multi-channel Kalman smoother (MCKS) will be proposed to acquire enhanced vital sign waveforms for subsequent accurate estimates of RR and HR in this paper. Inspired by the outlier-robust Kalman filter technique [26], [27], the MCKS is proposed to address the abnormality caused by the RBM and acquire the improved phase histories for further vital signs estimation.

With respect to the mth target, we stack $\tilde{\phi}_{m,p}(\tau)$, which denotes a filtered version of the phase history $\phi_{m,p}(\tau)$, into a vector as $\mathbf{y}_m(\tau) = \left[\tilde{\phi}_{m,1}(\tau), \ldots, \tilde{\phi}_{m,P}(\tau)\right]^T$. Ideally, $\{\tilde{\phi}_{m,p}(\tau)\}_{p=1}^P$ should have an identical vital signs

waveform except individual noise in each channels after the notch filter. We acquire the phase history vector $\mathbf{y}_m(l) = \left[\tilde{\phi}_{m,1}(l), \ldots, \tilde{\phi}_{m,P}(l)\right]^T$ at the lth chirp, and can denote the vector as,

$$\mathbf{y}_m(l) = a \times x_m(l) + \boldsymbol{\epsilon}_m(l), \quad l = 1 \ldots, L_0, \tag{15}$$

where $a = 2\pi f_c \times [1, \ldots, 1]^T \in \mathcal{R}^{P \times 1}$ is a vector, a scalar $x_m(l) = 2R_m(l)/c$ denotes the true time-delay value from the mth target at the lth chirp, and $\boldsymbol{\epsilon}(l) \in \mathcal{R}^P$ is the additive noise in the multiple channels. L_0 is the total number of received chirps. According to Eq.(15), the observed phase histories in multiple channels can be regarded as a true phase history waveform plus noises.

To alleviate the effects of outliers and noises in the multiple channels, we propose a novel Bayesian algorithm that treat the weights associate with each observation data samples probabilistically. In particular, we introduce a scalar weight $w_m(l)$ for each observed data sample vector to cope with outliers, motivated by references [26], [27]. We introduce a scaler $w_m(l)$ to weight the variances of all the elements in observed data sample vector, and acquire,

$$p\left(\mathbf{y}_m(l)|x_m(l), w_m(l), \boldsymbol{\Sigma}_m\right) \sim \mathcal{N}\left(\mathbf{y}_m(l)|ax_m(l), \boldsymbol{\Sigma}_m/w_m(l)\right), \tag{16}$$

where $\boldsymbol{\Sigma}_m = \text{diag}(\boldsymbol{\sigma}_m)$, which represents the covariance matrix for observation noise, is a diagonal matrix with $\boldsymbol{\sigma}_m = [\sigma_{m,1}, \ldots, \sigma_{m,P}]^T$, and will be estimated in the model. In addition, a Gamma prior distribution is imposed on the weight w_l as,

$$w_m(l) \sim \text{Gamma}\left(w_m(l)|a_0, b_0\right), \tag{17}$$

where a_0 and b_0 are hyperparameters respectively.

Considering the fact that true time delay should be slowly changing over chirps, and thus we introduce the random walk technique [28], and model the state equation as

$$x_m(l+1) = x_m(l) + \varepsilon_m(l), \quad l = 1, \ldots, L_0, \tag{18}$$

where $x_m(l+1)$ is the time delay at the $(l+1)$th chirp for the mth target, and $\varepsilon_m(l)$ is an additive noise. Without loss of generality, a Gaussian prior is considered to model this noise, and thus it can be expressed by,

$$\varepsilon_m(l)|v_m \sim \mathcal{N}\left(\varepsilon_m(l)|0, v_m\right), \tag{19}$$

where v_m is the variance of state noise for the mth target.

For the L_0 observed sample vectors, we perform the log evidence of the data samples observed, i.e., $\log p(\mathbf{y}_m(1:L_0), x_m(1:L_0), w_m(1:L_0))$ to estimate the posterior distributions of the random variables and parameter values.

We can treat this problem as an Expectation Minimization-like (EM) learning problem [29]. The expectation of the complete data likelihood should be taken with respect to the true posterior distribution of all hidden variables

$(x_m(1 : L_0), w_m(1 : L_0))$. However, since this is an analytically intractable expression, we make a factorial approximation of the true posterior as follows,

$$p\left(x_m(1:L_0), w_m(1:L_0)\right)$$
$$= \prod_{l=1}^{L_0} p\left(w_m(l)\right) p\left(x_m(l+1)|x_m(l)\right) p\left(x_{m,1}\right). \quad (20)$$

This factorization of $x(1 : L_0)$ takes the influence of each $x(l)$ from within its Markov blanket into consideration. Based on this factor approximation, all resulting posterior distributions over hidden variables become analytically tractable. We can provide the EM update equations from the manipulations of Gaussian and Gamma distributions, and the specific derivation steps are provided in Appendix.

The parameter of the weight in the lth chirp is given by,

$$\left\langle \hat{w}_m(l) \right\rangle = \frac{a_0 + P/2}{\sum_{p=1}^{P} \frac{1}{2\langle \sigma_{m,p} \rangle} \left(y_{m,p}(l) - 2\pi f_c \hat{x}_m(l)\right)^2 + b_0}. \quad (21)$$

The update equation of weight reveals that if the prediction error of $\sum_p (y_{m,p}(l) - 2\pi f_c \hat{x}_m(l))^2$ in $\mathbf{y}_m(l)$ is so large that it dominates the denominator, then the weight $\left\langle \hat{w}_m(l) \right\rangle$ of that data sample vector will be very small. As this prediction error term in the denominator goes to ∞, $\left\langle \hat{w}_m(l) \right\rangle$ approaches 0. If $\mathbf{y}_m(l)$ has a very small weight $\left\langle \hat{w}_m(l) \right\rangle$, the influence of the data sample vector $\mathbf{y}_m(l)$ will be downweighted by $\left\langle \hat{w}_m(l) \right\rangle$, when predicting $\hat{x}_m(l)$, at the lth chirp. This is the main reason why the proposed robust Kalman smoother has the capability of cope with the outliers that may caused by the RBMs.

Once these accurate time delay $\left\langle \hat{x}_m(l) \right\rangle$ is estimated at the lth chirp with respect to the mth target, and we obtain its desired phase histories as

$$\hat{\phi}_m(l) = 2\pi f_c \left\langle \hat{x}_m(l) \right\rangle, \quad m = 1, \dots, M. \quad (22)$$

The vital signs detection can be acquired based on this improved phase history.

In conclusion, the proposed MCKS weights the variances of all the elements in the observation data samples which are the phase histories extracted from multiple channels, and then updates the hidden variables through the EM algorithm. For the samples with outliers, its corresponding weight is relatively small in the estimation to alleviate the effect of the sample. The states are updated synchronously according to these weight values and we can finally achieve an optimal estimate of the phase histories.

B. VITAL SIGNS DETECTION BASED ON REGIONAL HIDDEN MARKOV MODEL

Unlike a simple Doppler-FFT on the phase histories for vital signs detection, a novel RHMM is proposed to acquire accurate estimates of the RR and HR by exploiting the underlying slowly-varying characteristics of the physiological vital signs in this section, motivated by frequency tracking techniques. we introduce the hidden Markov chain to model the slowly-varying RR and HR.

A collection $\mathbf{\Gamma}$ related to HMM can be firstly represented as,

$$\mathbf{\Gamma} = (\mathbf{\Psi}, \mathbf{\Omega}, \boldsymbol{\eta}_0), \quad (23)$$

where $\mathbf{\Psi}$ and $\mathbf{\Omega}$ denote the state transition matrix and observation probability matrix respectively, and $\boldsymbol{\eta}_0$ represents the initial probability. Once this collection $\mathbf{\Gamma}$ is known, the entire HMM is also determined. In the HMM-based frequency tracking, the number of hidden states is often equal to the length of frequency units K_0, and a large amount of computation for the state transition matrix is requisite. However, since RR and HR are confined to a limited frequency range, such as $f_r \in [0.1, 0.5]$ Hz and $f_h \in [0.8, 3.0]$ Hz, it is almost impossible that they move out of the ranges. Therefore, it is not necessary to spend time for the calculation of the probabilities of these impossible state transitions. In this paper, an RHMM, which takes full advantages of the effective frequency ranges of RR and HR has the capability of achieving the fast acquisition of vital signs with the smaller number of hidden states.

A short time Fourier transform (STFT) with the window length of K_0 and sliding window length of W_0 is firstly performed on the one-dimensional phase histories from the mth target, and then a time-frequency diagram in one data block $P_s^m \in \mathcal{C}^{K_0 \times N_0}$ with $N_0 = \lfloor (L_0 - W_0)/(K_0 - W_0) \rfloor$ can be obtained. The Doppler frequency interval is thus expressed as f_{PRF}/K_0. In accordance with the ranges of RR and HR, the numbers of hidden states can be easily calculated by

$$K_1 = \left\lfloor \frac{0.4K_0}{f_{\text{PRF}}} \right\rfloor, \quad K_2 = \left\lfloor \frac{2.2K_0}{f_{\text{PRF}}} \right\rfloor, \quad (24)$$

with $K_1, K_2 \ll K_0$.

Owing to slowly-varying RR and HR, it is reasonable that the adjacent states would have high transition probabilities. Therefore, a Gaussian function with zero mean and variance of σ_x^2 which can be represented as $\mathcal{N}\left(x|0, \sigma_x^2\right)$ is introduced to model the state transitions. The transition probability from the ith hidden state to the jth state can be given by

$$g_{ij} = \frac{1}{\sqrt{2\pi}\sigma_x} \int_{f_j}^{f_{j+1}} e^{-\frac{(f-\bar{f}_i)^2}{2\sigma_x^2}} df \quad i, j > 0, \quad (25)$$

where $\bar{f}_i = (f_i + f_{i+1})/2, i, j \le K_1$ in the RR case, and $i, j \le K_2$ in the HR case.

By performing the normalization on these probabilities, we have the (i, j)th element of ψ_{ij} in the state transition matrix $\mathbf{\Psi}$ as

$$\psi_{ij} = \frac{g_{ij}}{\sum_j g_{ij}}. \quad (26)$$

The observation probability is obtained by normalizing the power spectrum $\mathbf{p}_{sn}^m$ with the nth column in the time-frequency diagram $\mathbf{P}_s^m$, which can be expressed as

$$\omega_{in}^m = \mathbf{Pr}\left(x_n^m|f_i\right) = \frac{\mathbf{p}_{sn}^m(i)}{\sum_i \mathbf{p}_{sn}^m(i)}, \quad (27)$$

Algorithm 1 The Process for the Estimates of RR and HR With Viterbi Algorithm

---

Input: Ψ, Ω, ξ
Output: $\mathbf{S}^*$

  for $q = 1; q = q + 1$ (q denotes the currently processed block number) **do**

    Step 1 : Initialize the maximum local state probabilities parameters $\delta_{q(n)}(i)$ and corresponding state storage index $\theta_{q(n)}(i)$ in the state space ($q(n)$ denotes the nth time point of the qth data block and $n \in [1, 2, \ldots, N_1]$):
    if $q = 1$ **then**

$$\delta_{q(1)}(i) = \eta_{0i} \cdot \omega_{iq(1)}, \ \theta_{q(1)}(i) = 0 \ i \in [1, 2, \ldots, K_1]$$

    else

$$\delta_{q(1)}(i) = \delta_{q-1(N_1)}(i), \ \theta_{q(1)}(i) = \theta_{q-1(N_1)}(i)$$

    end if
    Step 2: Recursive backwards:
    for $n = 2, 3, \ldots, N_1$ **do**

$$\delta_{q(n)}(j) = \max_{1 \le i \le K_1} \left[\delta_{q(n-1)}(i)\psi_{ij} \right] \omega_{iq(n)}$$
$$j \in [1, 2, \ldots, K_1]$$
$$\theta_{q(p)}(j) = \arg\max_{1 \le i \le K_1} \left[\delta_{q(p-1)}(i)\psi_{ij} \right] \ j \in [1, 2, \ldots, K_1]$$

    end for
    Step 3: Estimate the state $i_{q(N_1)}$ at time $q(N_1)$ by maximizing $\delta_{q(N_1)}(j)$:

$$s^*_{q(N_1)} = \arg\max_{1 \le j \le K_1} \left[\delta_{q(N_1)}(j) \right]$$

    Step 4: Optimal path backtracking:
    for $n = N_1 - 1, \ldots, 1$ **do**

$$s^*_{q(n)} = \theta_{q(n+1)}\left(s^*_{q(n+1)}\right)$$

    end for
    Step 5: Obtain the optimal state sequence $\mathbf{S}^* = \left(s^*_{q(1)}, s^*_{q(2)}, \ldots, s^*_{q(N_1)}\right)$
  end for

---

where $i = 1, \ldots K_1$ in the RR case, $i = 1, \ldots K_2$ in the HR case, and $n = 1, \ldots, N_0$. x^m_n is an element in the vector $\mathbf{p}^m_{sn}$, and ω^m_{in} represents the probability that the observation result is x^m_n with the hidden state of f_i. It should be pointed that the size of the transition matrix is reduced to $K_1 \times K_1$ in RR and $K_2 \times K_2$ in HR due to the confined frequency ranges in RHMM, compared to the matrix with the size of $K_0 \times K_1$ and $K_0 \times K_2$ in the traditional HMM.

Without loss of generality, the initial probability η_0 is assumed to follow uniform distribution. To be detail, in the RR case, $\eta_0 = [\eta_{01}, \ldots, \eta_{0K_1}] = [1/K_1, \ldots, 1/K_1] \in \mathcal{R}^{K_1 \times 1}$ and in the HR case, $\eta_0 = [1/K_2, \ldots, 1/K_2] \in \mathcal{R}^{K_2 \times 2}$. Once the collection Γ is given, and the entire RHMM is determined.

Given an RHMM, the commonly used Viterbi algorithm is taken into consideration for the fast acquisition of vital signs [28]. Instead of directly performing the Viterbi algorithm to the RHMM on the entire $\mathbf{P}^m_s$ at one time, which would have an amount of computational complexity, We divide $\mathbf{P}^m_s$ with the size of $K_1 \times N_0$ into Q blocks with the size of $K_1 \times N_1$ and sequentially perform the Viterbi algorithm on each block, rather than treating them independently. The detailed process is presented in Algorithm 1 for the estimates of both RR and HR.

C. SUMMARY OF THE PROPOSED VITAL SIGNS DETECTION SCHEME

The proposed scheme is summarized in Algorithm 2.

Algorithm 2 Summary of the Proposed Vital Signs Detection Scheme

---

Input: The received signal $s^p_{\text{RX}}(t)$ of LFMCW radar, $p \in [1, 2, \ldots, P]$
  Step 1 : Obtain the beat signal $s^p_b(t)$ by mixing the received signal $s^p_{\text{RX}}(t)$ with the transmitted signal $s_{\text{TX}}(t)$, then perform FFT over the beat signal to acquire the associated phase histories $\phi_{m,p}(\tau)$ ($m \in [1, 2, \ldots, M]$) from the targets' range bins.
  Step 2: Unwrap the phase histories and perform a notch filter on them to remove the constant phase differences across channels and acquire the results $\tilde{\phi}_{m,p}(\tau)$.
  Step 3: Perform MCKS on $\{\tilde{\phi}_{m,p}(\tau)\}^P_{p=1}$ and obtain the improved phase history $\hat{\phi}_m$.
  Step 4: Perform STFT on $\hat{\phi}_m$ and obtain the RHMM based on the time-frequency diagram P^m_s. Divide P^m_s into Q blocks and perform Viterbi Algorithm on the RHMM to acquire the estimates of both RRs and HRs of all the targets.
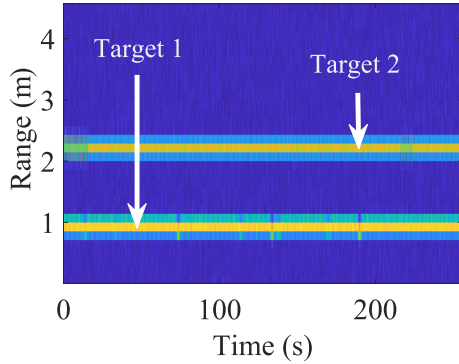**Output:** Estimate RRs and HRs of multiple targets.

IV. SIMULATION RESULTS

In the simulations, we assume two targets with ranges of 0.9 m and 2.2 m are in front of a 77GHz LFMCW radar system, and the number of receive channels P is 4 with the interval of $\lambda/2$. RBMs are applied as a series of triangular pulses used in [18]. The maximum amplitudes of RBMs lie in [5, 20]cm, and their durations vary in [1, 4]s. In this case, the range of the body movement speed is [1.25, 20] cm/s. The data collection time is 240 s, and the ratio of the RBM duration over the collection time is 20%. For the closer target, the ranges of slowly-varying RR and HR are [18, 22] bpm and [75, 85] bpm respectively, while the corresponding farther target's ranges are [16, 20] bpm and [65, 75] bpm. The STFT

TABLE 1. Parameters for the LFMCW Radar system.

Parameters	Definition	Values
f_{PRF}	Pulse repetition frequency for LFMCW radar	20 Hz
f_c	Carrier frequency	77 GHz
B	Bandwidth	2GHz
F_s	Sampling rate	5 MHz
T	Pulse duration	50 μs
FFT_r	Range FFT points	128

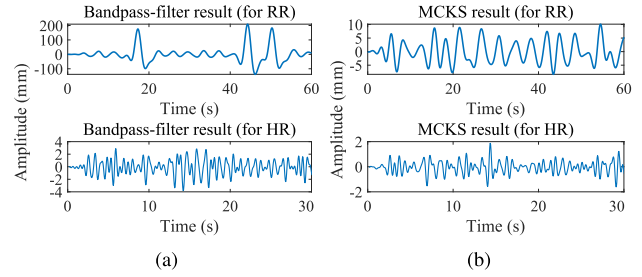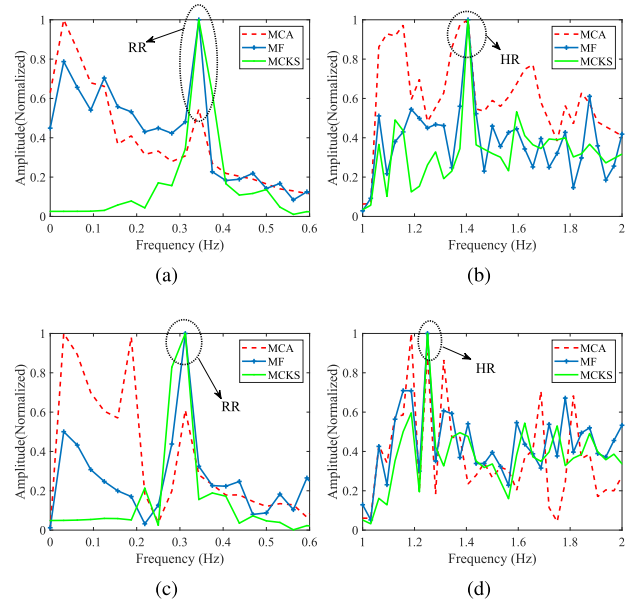**FIGURE 5.** Range-FFT result of one channel in the simulation.

FIGURE 6. Process results of the closer target. (a) Bandpass-filter results of one channel. (b) MCKS results.

FIGURE 7. Spectra around the RR and HR of the results obtained by MCKS, MCA and MF methods. (a) RR results of the closer target. (b) HR results of the closer target. (c) RR results of the farther target. (d) HR results of the farther target.

window length of 12 s with $K_0 = 240$ is used, and the sliding window of 1.5 s with $W_0 = 30$ which is approximately half a respiration cycle is considered. Without loss of generality, additive noise is considered with the SNR of 10 dB. Following the real experiments, the radar parameters in the simulations are shown in Table 1. The bandwidth of the transmitted LFMCW waveform is 2 GHz with a duration of 50 μs, which corresponds to the range resolution of 7.5 cm. The sample rate is 5 MHz, and the number of samples in each chirp is 128. The pulse repetition frequency (PRF) is 20 Hz, which conforms to the Nyquist sampling theorem for the perfect reconstruction of the RR and HR waveforms.

A. PERFORMANCE COMPARISONS IN THE PROPOSED MCKS METHOD

In this simulation, We firstly perform the FFT on the beat signals, and then acquire the associated range profile, as shown in Fig.5. Two targets are easily detected and separated due to the high range resolution of 7.5 cm in this LFMCW radar system. Thus the four-channel phase histories in the corresponding range bins are extracted for the subsequent vital signs detection.

The notch filter with the notch width of 0.02 is performed to remove these DC components caused by the diverse spatial locations. A bandpass filter with the ranges of [0.1, 0.5] Hz for RR and [0.8, 3.0] Hz for HR is performed on the phase histories of all the channels before the MCKS operation. The initial parameters of the Gamma prior distribution in Eq.(17) are $a_0 = 1$ and $b_0 = 1$. In the RR case, the variance of state noise v_m in Eq.(19) is 0.1 and the covariance matrix for observation noise Σ_m in Eq.(16) is diag($[0.1, 0.1, 0.1, 0.1]^T$) while $v_m = 1$ and $\Sigma_m = $ diag($[1, 1, 1, 1]^T$) in the HR case.

Fig.6(a) shows the bandpass-filter results of phase histories in the reference channel. It can be observed that there exist significantly abnormal values similar to triangular pulses on the phase histories, which are caused by large-scale RBMs in the data collection. By performing the proposed MCKS method, we weight the variances of all the elements in the observed data sample vector, and the weight values corresponding to the triangular pulses are suppressed by a periodic update. Thus the outliers are effectively mitigated, and the acquired vital signs waveforms are much smoother. The corresponding amplitude range is confined into 10 mm for RR and less than 2 mm for HR, shown in Fig.6(b).

We perform STFT on the phase history waveforms so that a time-frequency diagram can be acquired. Fig.7 shows two slides from the time-frequency diagram. It is found that the spectra based on the proposed method have the highest peak in the true locations in both RR and HR, however, there are still some large interferences around the RR in the MCA and state-of-the-art MF methods [18].

TABLE 2. Local SNRs comparisons around the RR and HR.

		Channel 1	Channel 2	Channel 3	Channel 4	MCA	MF	MCKS (One Channel)	MCKS (Four Channels)
RR	Target 1	0.1801	0.1276	0.1026	0.1767	0.2394	3.2826	4.6484	**8.7125**
	Target 2	-1.3773	-0.8557	-2.0313	-1.3695	-1.3501	2.0322	3.5771	**6.3724**
HR	Target 1	1.5670	2.1102	2.8354	1.0677	3.2775	3.3965	3.2666	**3.9063**
	Target 2	1.5609	0.7316	0.6128	0.1727	1.8554	1.9414	1.7698	**2.3634**

To quantify the performance, we introduce a local SNR (LSNR) as the performance index, which is defined as,

$$\chi = \frac{\int_{f_0-f_{w1}}^{f_0+f_{w1}} |\mathbf{Y}(f)|^2 \, df}{\int_{f_0-f_{w2}}^{f_0+f_{w2}} |\mathbf{Y}(f)|^2 \, df - \int_{f_0-f_{w1}}^{f_0+f_{w1}} |\mathbf{Y}(f)|^2 \, df}, \quad (28)$$

where $\mathbf{Y}(f)$ represents the amplitude of the frequency spectrum corresponding to frequency f and f_0 denotes the RR and HR respectively in the two cases. f_{w1} is 0.06 Hz and f_{w2} is 0.20 Hz.

Table 2 shows the performance comparisons of the LSNR. To verify the advantage of multi-channel collections, we also perform the MCKS with single-channel data for comparison, exploiting one of the reception channels. It can be observed that the MCKS method in one reception generally has higher LSNRs in the RR and HR waveforms, compared to these in each channel. It seems that the LSNR improvements in the RR waveforms are higher than those in the HR waveforms in the proposed method. It is also observed that the LSNRs in the MCKS method with a single-channel data still have nearly 1.0 dB improvement, compared to these in the MCA and MF methods in the RR waveforms, whereas it is slightly lower than these in the MCA and MF methods in the HR waveforms. However, the MCKS method with four reception channel data has the highest gains in both closer target and farther target for the reason that the LSNRs in the MCKS method with four channels have the largest values. In the RR estimate, the result of MCKS with four channels is even up to 7.5 dB higher than that of the MCA method, and about 4.0 dB higher than that of the MF method. Compared to the MCKS with one channel, the LSNR gain is more than 2.5 dB. In the HR estimate, the MCKS with four channels has a slight increase in LSNR which is approximately 0.5 dB. Besides, it is found that the proposed method has higher SNR gains in the RR estimate, compared to that in the HR estimate. The main reason may be the interferences caused by the large-scale RBMs mainly have the low-frequency components whose range coincides with RR. The estimated results are shown in Fig.7.

B. PERFORMANCE COMPARISONS IN THE PROPOSED RHMM METHOD

In this section, we perform the STFT on the improved robust-outlier waveforms and acquire its time-frequency diagrams. The sizes of each block are $K_1 = 128$ and $N_1 = 5$, and the vital signs detection result will be updated per 5 chirps. The σ_x in Eq.(25) is set to 1 by default. The corresponding
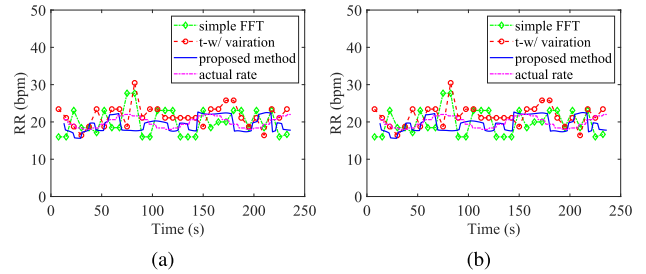

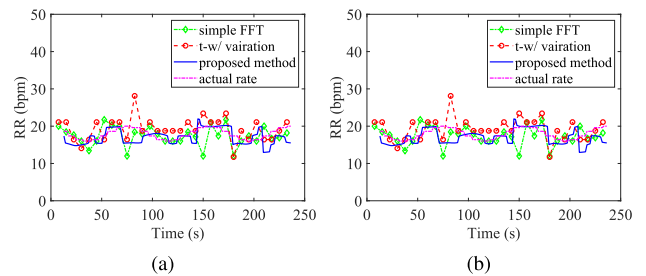**FIGURE 8.** Estimated RR and HR results of the closer target. (a) RR results. (b) HR results.

FIGURE 9. Estimated RR and HR results of the farther target. (a) RR results. (b) HR results.

updated rates of estimate results would be 7.5 s duo to the sliding window of 1.5 s so that the fast acquisition of vital sign detection can be achieved. The estimate resolution is approximately 0.0041Hz and is equivalent to 0.25 bpm due to the STFT window length $K_0 = 240$.

The estimate results of the closer and farther targets' RRs and HRs are shown in Fig. 8 and Fig. 9, respectively. Fig.8 shows the estimated results of RR and HR acquired by the proposed RHMM for the target with the closer range. It is observed that the estimates of RR are smoother due to the exploitation of the slowly-varying characteristics, and are quite closer to the ground truth, compared to the results acquired by the simple FFT and the time-window-variation technique [30], which treat the estimates of RR and HR independently in time. It is clear that the estimated values of HR also closely match the true ones. Similar results are also obtained for the farther target, shown in Fig.9.

To quantify the performances, we introduce the error rate β as the performance index, and provide the definition by,

$$\beta = \frac{|\text{Rate}_{\text{Est}} - \text{Rate}_{\text{Truth}}|}{\text{Rate}_{\text{Truth}}} \times 100\%. \quad (29)$$

For the RR estimates, the average error rates β in the simple FFT method and time-window-variation method are 16.78% and 10.03% for the target with a closer range, respectively, and these values slightly increase to 16.82% and 10.25% for the farther target. However, the average error rates in the proposed RHMM are respectively reduced to 7.84% and 8.79%, even though 20% RBM duration with the amplitude up to 10 cm. Besides, the average error rates are respectively 1.58% and 2.08% in the HR estimation, compared to 6.31% and 6.48% in the simple FFT method, and 4.97% and 5.68% in the time-window-variation method.

To further analyze the performance of alleviating the RBMs, we also use the phase history waveforms acquired from the MCA operator and MFp method to conduct the estimates of RR and HR. Results are shown in Table 3, it can be observed that the estimates results acquired after the MCKS processing are better than those in MCA and MF cases overall. Besides, the proposed RHMM also has lower error rates in both MCA and MF cases.

TABLE 3. Performance comparisons in the RR and HR estimation in simulations.

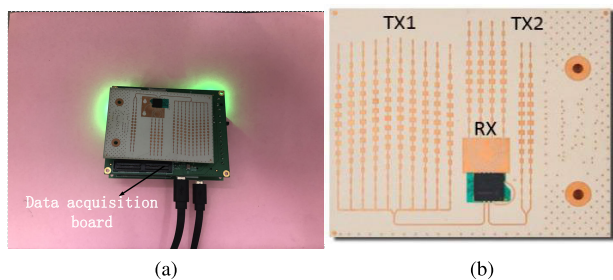|		Pre-method	Simple FFT	T-w/ variation	RHMM
RR	Target1	MCA	21.32%	13.98%	**9.55%**
		MF	19.03%	11.94%	**8.46%**
		MCKS	16.78%	10.08%	**7.84%**
	Target2	MCA	22.36%	15.33%	**10.15%**
		MF	20.17%	12.78%	**9.13%**
		MCKS	16.82%	10.25%	**8.79%**
HR	Target1	MCA	9.44%	7.62%	**3.11%**
		MF	8.35%	6.57%	**2.74%**
		MCKS	6.31%	4.97%	**1.58%**
	Target2	MCA	9.87%	8.45%	**3.53%**
		MF	8.91%	7.42%	**2.95%**
		MCKS	6.48%	5.68%	**2.08%**

FIGURE 10. Photograph of the Cal77A2T4R radar system. (a) Overall appearance. (b) Antenna arrangement.

V. EXPERIMENT RESULTS

Experiments are performed based on the Cal77A2T4R radar system which has two transmitters (Tx) and four receivers (Rx) with the carrier frequency of 77 GHz. The specific structure is shown in Fig.10. The gains of Tx1 and Tx2 antennas are respectively 19 dBi and 15 dBi, and the gain of received Rx is 13 dBi. The maximum output power is 13 dBm, and the noise figure of Rx antenna is 12 dB. We used Tx1 antenna and all the four Rx antennas in our experiments to collecting
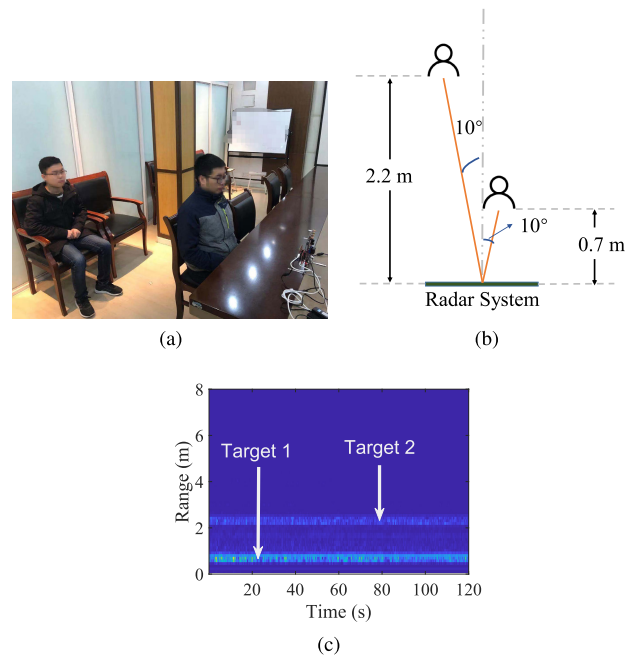

FIGURE 11. Real experiment demonstration. (a) Experimental scenario. (b) The illustration of the objects' placement. (c) Range profile of the reference channel.

raw data. The half-power beamwidth of the Tx1 and Rx antennas are 45° and 70° respectively. Radar parameters are shown in Table 1.

A. EXPERIMENT DESCRIPTION

The experimental scenario is shown in Fig.11(a)-(b), two healthy young men with the ages of [20, 30] sat in front of the radar with different ranges, and the azimuths of these two objects are approximately 10 degrees on different sides. The data collection time is 240 seconds. For the performance comparisons, a Gladstone YK-83C finger-clip contact-type sensor is used to acquire the reference RRs and HRs. The received signals in the four antennas are acquired, and one of the range profiles is shown in Fig.11(c). The distances between the targets and radar are approximately 0.7 m and 2.2 m respectively. Two targets are easily separated in range due to the range resolution of 7.5 cm.

TABLE 4. Normal and abnormal vital signs for different ages.

Age	RR		HR	
	normal	abnormal	normal	abnormal
Neonate	30-60	>60	100-160	>200 or <65
Infant	30-40	>60	90-150	>190 or <60
2-5 years	20-30	>50	85-130	>180 or <55
5-12 years	15-20	>40	80-120	>170 or <50
>12 years	12-16	>35	60-100	>160 or <45

For comparison, we list the normal and abnormal values of RR and HR at different ages [31], [32], as shown in Table 4. It is observed that the RR and HR will increase or decrease in response to a variety of changes, including exercise,

body temperature, emotional triggers, and body position. The selected frequency intervals of [0.1,0.5]Hz for RR and [0.8,3.0] Hz for HR almost cover the entire range according to the list above.

B. EXPERIMENTS IN FREE-RBM SCENARIO

To show the adaption and advantage of the proposed method in practice, we first take the experiment in a free-RBM scenario into consideration. That is, two objects are almost quasi-stationary during data collection. The phase histories of the two targets in the corresponding range bins are firstly extracted respectively, and then the notch filter is performed. Fig.12 shows the unwrapped phase histories and phase histories after the notch filter for both closer and farther targets. It is observed that these waveforms are quite smooth in this free-RBM scenario. Then the MCKS method is performed on the phase histories, and the initial hyper-parameters are followed in Section IV-A.
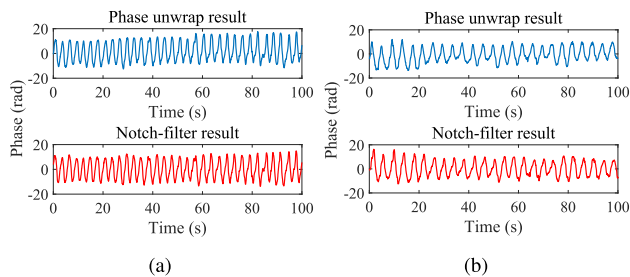

FIGURE 12. Phase unwrapping and notch-filter results of the reference channel. (a) Closer target's results. (b) Farther target's results.

Fig.13 shows improved vital signs phase history waveforms based on the MCKS method. It can be observed that these peaks in the waveforms can be distinguished clearly, and the amplitudes of the closer target's vital signs are larger. The MCKS results are almost consistent with those of bandpass filtering in this free-RBM scenario.
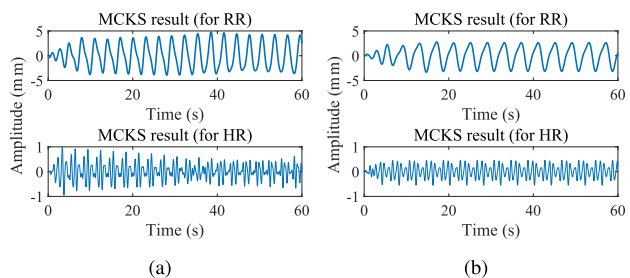

FIGURE 13. Estimated results based on the proposed MCKS method. (a) Closer target's results. (b) Farther target's results.

Fig. 14 shows the performance comparisons of error rates for the two targets. All the methods have satisfactory performances, and estimated rates of RR and RR are quite close to the ground truth. However, it is observed that the proposed RHMM has the result closest to the reference frequencies with minimal fluctuations. Similarly, the average errors are used to evaluate the performance of RR and RR estimation. For the RR estimates, the average error rates β in the
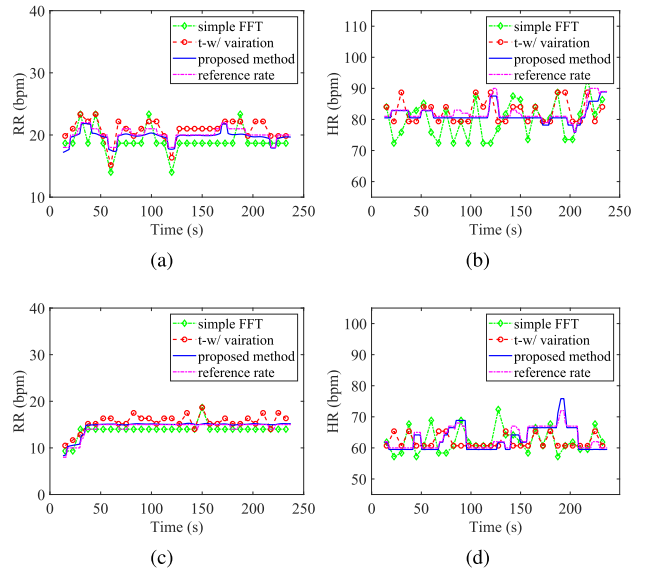

FIGURE 14. Estimated results of RR and HR based on the proposed RHMM method. (a) Closer target's RR. (b) Closer target's HR.(c) Farther target's results. (d) Farther target's HR.

simple FFT method and time-window-variation method are 8.38% and 6.61% for the target with a closer range, respectively, and these values slightly increase to 8.39% and 6.66% for the farther target. However, the average error rates in the proposed RHMM are respectively reduced to 1.91% and 2.12%, even less than 1 bpm. Besides, the average error rates are respectively 1.02% and 1.31% in the HR estimation, compared to 6.67% and 6.83% in the simple FFT method, and 2.83% and 3.30% in the time-window-variation method.

Similarly, we also perform the MCA and MF methods over the phase histories of the four channels and then conduct the detection of the vital signs. The comparisons of results are listed in Table 5. All these three methods acquire comparable results, however, the proposed method has slightly better results than these in the other two methods.

TABLE 5. Performance comparisons in the RR and HR estimation in free-RBM scenario.

		Pre-method	Simple FFT	T-w/ variation	RHMM
RR	Target1	MCA	8.97%	6.92%	**2.00%**
		MF	8.91%	6.84%	**1.98%**
		MCKS	8.38%	6.61%	**1.91%**
	Target2	MCA	9.27%	7.01%	**2.41%**
		MF	8.94%	6.90%	**2.35%**
		MCKS	8.39%	6.66%	**2.22%**
HR	Target1	MCA	6.81%	2.99%	**1.17%**
		MF	6.77%	2.92%	**1.11%**
		MCKS	6.67%	2.83%	**1.02%**
	Target2	MCA	6.96%	3.39%	**1.38%**
		MF	6.91%	3.35%	**1.34%**
		MCKS	6.83%	3.30%	**1.31%**

C. EXPERIMENTS IN RBM SCENARIO

In this subsection, two objects perform RBMs with the duration of 2 s in every fixed time interval (12 s for the closest target and 10 s for the farther target), respectively. The RBM
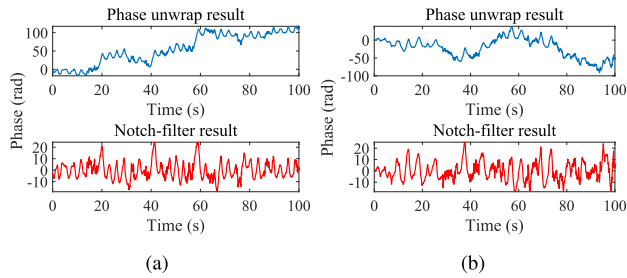
FIGURE 15. Phase unwrapping and notch-filter results of the reference channel. (a) Closer target's results. (b) Farther target's results.

amplitude is approximately 10 cm. The data collection time is 240 s. It suggests that we will acquire the 20 and 24 times of the RBMs for closer and farther targets during the entire data collection period, respectively. Fig.15 shows the phase histories after unwrapping and notch-filter. Compared to Fig.12, it is observed that phase histories show clear derivations from the normal values, which can be viewed as outliers and be possibly caused by the RBMs.
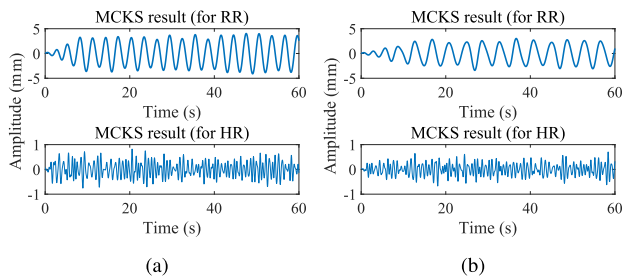

FIGURE 16. Estimated results based on the proposed MCKS method. (a) Closer target's results. (b) Farther target's results.

Fig.16 shows the improved vital signs phase histories after performing the multi-channel MCKS method. It is observed that the outliers or abnormies are mitigated and suppressed, and the improved waveforms become smoother.

The performance comparisons of the three methods are shown in Fig.17. The RHMM results have the least fluctuations and are closest to the reference values due to the reason that we exploit the slowly-varying characteristic of RR and HR to suppress the jumping of the tracking frequencies. For the closer target, the average error rates from RHMM are 7.18% (less than 2 bpm) for RR and 2.16% (less than 2 bpm) for HR, whereas the simple FFT has the rates of 18.36% for RR and 9.91% for HR, and the time-window-variation technique is 10.06% for RR and 5.55% for HR. For the farther target, the RHMM error rates are 8.50% and 2.36% respectively, compared to 21.09% and 10.31% in simple FFT and 10.50% and 6.97% in time-window-variation method, as shown in Table 6.

D. EFFECT OF DIFFERENT RBM FEATURES

In this subsection, quantitative analyses are taken based on the various amplitude, duration, and time intervals of RBM, respectively. Firstly, the amplitudes of RBM vary from 5 cm
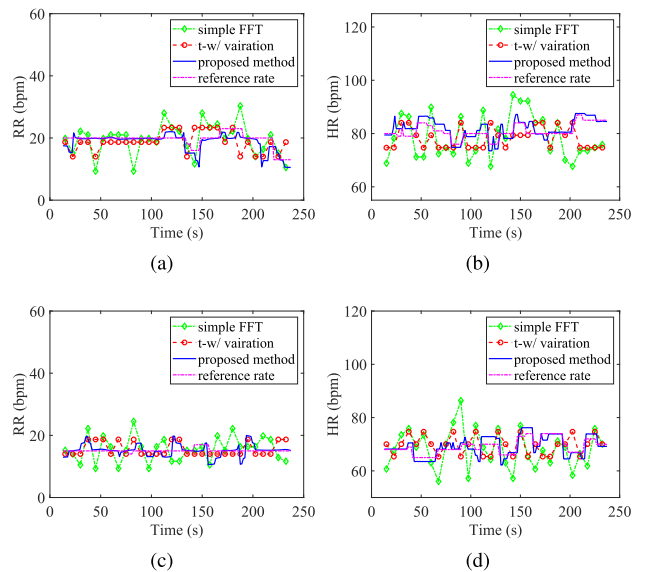

FIGURE 17. Estimated results of RR and HR based on the proposed RHMM method. (a) Closer target's RR. (b) Closer target's HR.(c) Farther target's results. (d) Farther target's HR.

TABLE 6. Performance comparisons in the RR and HR estimation in RBM scenario.

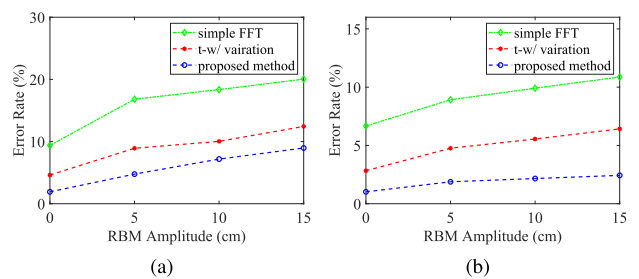|		Pre-method	Simple FFT	T-w/ variation	RHMM
RR	Target1	MCA	24.78%	13.91%	**9.80%**
		MF	22.12%	12.85%	**8.84%**
		MCKS	18.36%	10.06%	**7.18%**
	Target2	MCA	28.03%	14.86%	**11.65%**
		MF	25.87%	13.56%	**10.59%**
		MCKS	21.09%	10.50%	**8.50%**
HR	Target1	MCA	14.21%	9.25%	**4.34%**
		MF	12.16%	8.18%	**3.29%**
		MCKS	9.91%	5.55%	**2.16%**
	Target2	MCA	14.35%	9.91%	**4.60%**
		MF	13.21%	8.89%	**3.47%**
		MCKS	10.31%	6.91%	**2.36%**

FIGURE 18. Performance comparisons of different RBM amplitudes. (a) RR result (b) HR result.

to 15 cm in the experiment, with the duration of 2 s and the fixed time interval of 12 s. The comparison curves of the three methods are shown in Fig.18. It can be observed that all the error rates of the three methods increase slightly with the improvement of RBM amplitude, and the proposed RHMM has the lowest error rates in each interval.

Then, we fixed the RBM amplitude to 10 cm and the time interval to 12 s, and the duration varied from 1 s to 5 s.
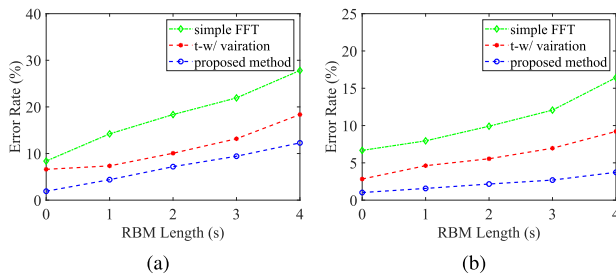
FIGURE 19. Performance comparisons of different RBM lengths. (a) RR result (b) HR result.
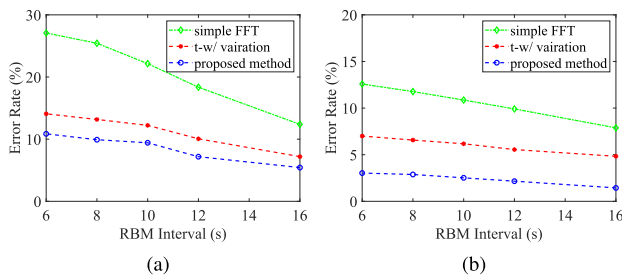

FIGURE 20. Performance comparisons of different RBM time intervals. (a) RR result (b) HR result.

Fig.19 shows the performance comparisons. The results are provided in Fig.18. It is found that accuracies of all three methods become worse with the increase of the RBM lengths, whereas the RHMM still has the lowest average error rates.

Finally, we change the time intervals with the RBM amplitude of 10 cm and the RBM duration of 2 s in the experiment. Estimated results are shown in Fig.20. It seems that it is difficult to estimate the vital signs with high accuracy when the RBM is very dense, especially using the simple FFT method(The average error rate is almost up to 30%). However, as the interval increases, the error rates show a downward trend, and the RHMM method has better performance. Similar results are also found in the farther target. In general, it is reasonable that the estimated performances of RR and HR seem confined to the RBM's amplitude and RBM's duration, whereas they seem to benefit from the time interval.

VI. DISCUSSION
The theoretical analysis, simulations, and experiments in the previous sections present a new signal processing scheme to detect vital signs. By observing the experiments results in some previous research [30], [33], [34], the accuracies in Section V can be considered reasonable. However, the study is based on several assumptions and has some limitations, which need to be discussed in this section.

Firstly, the vital signs model given in Eq.(7) is simplified as the superposition of sinusoidal signals based on the assumption that RR and HR are irrelevant. The reason is to simplify the analysis [9]. The displacements of the chest wall do not necessarily have sinusoidal waveforms and there is a coupling

relationship between the heart and lung so that the RR and HR are related [35], [36]. Therefore, further research should be conducted on the theoretical analysis for rigor.

Secondly, experiments are carried out under the scenarios where the objects are facing the radar system. In a real vital signs monitoring scenario, the human body may have more complex postures, such as lying down. Previous research has given a positive answer to the question that whether it is possible for vital signs detection from four sides of a human body [11]. On the other hand, it is worth mentioning that the RBMs have more complex forms, such as head-shaking, arm-moving, or body-turning, rather than just similar to triangle pulses. Therefore, the potential challenge that whether the proposed scheme is applicable in more complex environments needs further consideration.

Thirdly, the extraction of vital signs signal is based on the assumption that the objects do not cross the range gate. However, migration through range bins seems unavoidable to some extent due to the tiny resolution of 7.5 cm in real detection, especially under the large-scale RBMs environments. The range alignment preprocess technique is firstly performed before the subsequent MCKS and RHMM methods.

Besides, looking close back to Table 4, the selected frequency intervals fail to reach the highest abnormal values of the neonates and infants, for the reason that our work is based on the scenario in which the objects are healthy adults. To further verify the robustness of the proposed scheme, more experiments are necessary to be performed on the samples with different physical conditions at different ages.

Finally, there may be some unexpected emergencies during the vital signs monitoring process which make RR and HR change drastically. In the current development stage, the detection of these body anomalies requires a certain delay for the reason that we exploit the underlying slowly-varying characteristics of the RR and HR. For example, when a vital sign has a drastic change, the corresponding buffer time is approximately 15 s. Future solutions for the timeliness of emergency detection need to be researched out to realize more promising applications. Due to the above limitations of the proposed scheme, the suggested application scenario a relatively stable environment where the targets sit facing the radar system.

VII. CONCLUSION
This paper presented a novel vital signs detection scheme in the millimeter-wave radar system with multiple channels for the accurate estimates of the respiration rate (RR) and heart rate (HR) in the multiple targets with random body movements (RBMs) environment. In the proposed scheme, a 77 GHz radar system with the linear frequency modulated continuous wave was investigated to separate the multiple targets. The multi-channel Kalman smoother (MCKS) method was proposed to acquire improved robust-outlier phase history waveforms by effectively mitigating RBMs. Furthermore, the regional hidden Markov model was finally proposed to carry out accurate estimates of RR and HR by

exploiting the underlying slowly-varying characteristics of these vital signs for further mitigation of RBMs. Experiments demonstrated that the proposed MCKS method had the obvious gain increases of local signal-to-noise ratios in RR and HR over those in the multi-channel average and the matched filter methods, and the estimated errors in the proposed method were less than 2 beats per minute for both RR and HR with young men in the RBMs environment.

APPENDIX

The EM update equations in section III-A are given below.
red E-step:

Forward recursion,

$$\mathcal{N}\left(x_m(l)|\xi_m(l), v_m(l)\right) \propto \mathcal{N}\left(\mathbf{y}_m(l)|ax_m(l), \boldsymbol{\Sigma}_m/w_m(l)\right)$$
$$\times \mathcal{N}\left(x_m(l)|\xi_m(l-1), \langle v_m \rangle + v_m(l-1)\right), \quad (30)$$

$$\rightarrow \xi_m(l) = v_m(l)\left(\sum_{p=1}^{P} \frac{\langle w_m(l) \rangle}{\langle \sigma_{m,p} \rangle} y_{m,p}(l) + \frac{2\pi f_c \xi_m(l-1)}{\langle v_m \rangle + v_m(l-1)}\right), \quad (31)$$

$$\rightarrow v_m(l) = \left(\sum_{p=1}^{P} \frac{\langle w_m(l) \rangle}{\langle \sigma_{m,p} \rangle} + \frac{1}{\langle v_m \rangle + v_m(l-1)}\right)^{-1}, \quad (32)$$

$$\rightarrow \langle w_m(l) \rangle = \frac{a_0 + P/2}{\sum_{p=1}^{P} \frac{1}{2\langle \sigma_{m,p} \rangle}\left(y_{m,p}(l) - 2\pi f_c \xi_m(l)\right)^2 + b_0}. \quad (33)$$

Backward recursion,

$$\mathcal{N}\left(x_m(l)|\hat{\xi}_m(l), \hat{v}_m(l)\right) \propto \mathcal{N}\left(\hat{\xi}_m(l+1)|x_m(l), \langle v_m \rangle\right) \quad (34)$$
$$\times \mathcal{N}\left(x_m(l)|\xi_m(l), v_m(l)\right),$$

$$\rightarrow \hat{\xi}_m(l) = \xi_m(l) + \frac{v_m(l)}{v_m(l) + \langle v_m \rangle}\left(\hat{\xi}_m(l+1) - \xi_m(l)\right), \quad (35)$$

$$\rightarrow \hat{v}_m(l)$$
$$= v_m(l) + \frac{v_m(l)^2}{(v_m(l) + \langle v_m \rangle)^2}\left[\hat{v}_m(l+1) - (v_m(l) + \langle v_m \rangle)\right]? \quad (36)$$

$$\rightarrow \langle \hat{w}_m(l) \rangle = \frac{a_0 + P/2}{\sum_{p=1}^{P} \frac{1}{2\langle \sigma_{m,p} \rangle}\left(y_{m,p}(l) - 2\pi f_c \hat{\xi}_m(l)\right)^2 + b_0}. \quad (37)$$

M-step:

$$\langle \sigma_{m,p} \rangle = \frac{1}{l}\sum_{i=1}^{l} \langle w_m(i) \rangle \left(y_{m,p}(i) - 2\pi f_c\left\langle \hat{\xi}_m(i) \right\rangle\right)^2, \quad (38)$$

$$\langle v_m \rangle = \frac{2\pi f_c}{l}\sum_{i=1}^{l}\left(\left\langle \hat{\xi}_m(i) \right\rangle - \left\langle \hat{\xi}_m(i-1) \right\rangle\right)^2. \quad (39)$$

REFERENCES

[1] K.-M. Chen, Y. Huang, J. Zhang, and A. Norman, "Microwave life-detection systems for searching human subjects under earthquake rubble or behind barrier," *IEEE Trans. Biomed. Eng.*, vol. 47, no. 1, pp. 105–114, Jan. 2000.

[2] J. C. Lin, "Microwave sensing of physiological movement and volume change: A review," *Bioelectromagnetics*, vol. 13, no. 6, pp. 557–565, 1992.

[3] M. Forouzanfar, M. Mabrouk, S. Rajan, M. Bolic, H. R. Dajani, and V. Z. Groza, "Event recognition for contactless activity monitoring using phase-modulated continuous wave radar," *IEEE Trans. Biomed. Eng.*, vol. 64, no. 2, pp. 479–491, Feb. 2017.

[4] F. JalaliBidgoli, S. Moghadami, and S. Ardalan, "A compact portable microwave life-detection device for finding survivors," *IEEE Embedded Syst. Lett.*, vol. 8, no. 1, pp. 10–13, Mar. 2016.

[5] C. Li, V. M. Lubecke, O. Boric-Lubecke, and J. Lin, "A review on recent advances in Doppler radar sensors for noncontact healthcare monitoring," *IEEE Trans. Microw. Theory Techn.*, vol. 61, no. 5, pp. 2046–2060, May 2013.

[6] C. Li, Z. Peng, T.-Y. Huang, T. Fan, F.-K. Wang, T.-S. Horng, J.-M. Munoz-Ferreras, R. Gomez-Garcia, L. Ran, and J. Lin, "A review on recent progress of portable short-range noncontact microwave radar systems," *IEEE Trans. Microw. Theory Techn.*, vol. 65, no. 5, pp. 1692–1706, May 2017.

[7] J. Lin and W. Wu, "Vital sign radars: Past, present, and future," in *Proc. WAMICON*, 2014, pp. 1–4.

[8] C. Li, J. Ling, J. Li, and J. Lin, "Accurate Doppler radar noncontact vital sign detection using the RELAX algorithm," *IEEE Trans. Instrum. Meas.*, vol. 59, no. 3, pp. 687–695, Mar. 2010.

[9] J. Tu and J. Lin, "Respiration harmonics cancellation for accurate heart rate measurement in non-contact vital sign detection," in *IEEE MTT-S Int. Microw. Symp. Dig.*, Jun. 2013, pp. 1–3.

[10] C. Li and J. Lin, "Complex signal demodulation and random body movement cancellation techniques for non-contact vital sign detection," in *IEEE MTT-S Int. Microw. Symp. Dig.*, Jun. 2008, pp. 567–570.

[11] C. Li, J. Lin, and Y. Xiao, "Robust overnight monitoring of human vital signs by a non-contact respiration and heartbeat detector," in *Proc. Int. Conf. IEEE Eng. Med. Biol. Soc.*, Aug. 2006, pp. 2235–2238.

[12] X. Yu, C. Li, and J. Lin, "Noise analysis for noncontact vital sign detectors," in *Proc. IEEE 11th Annu. Wireless Microw. Technol. Conf. (WAMICON)*, Apr. 2010, pp. 1–4.

[13] G. Wang, J.-M. Munoz-Ferreras, C. Gu, C. Li, and R. Gomez-Garcia, "Application of linear-frequency-modulated continuous-wave (LFMCW) radars for tracking of vital signs," *IEEE Trans. Microw. Theory Techn.*, vol. 62, no. 6, pp. 1387–1399, Jun. 2014.

[14] H. Lee, B.-H. Kim, and J.-G. Yook, "Path loss compensation method for multiple target vital sign detection with 24-GHz FMCW radar," in *Proc. APCAP*, Aug. 2018, pp. 100–101.

[15] C. Li and J. Lin, "Random body movement cancellation in Doppler radar vital sign detection," *IEEE Trans. Microw. Theory Techn.*, vol. 56, no. 12, pp. 3143–3152, Dec. 2008.

[16] F.-K. Wang, T.-S. Horng, K.-C. Peng, J.-K. Jau, J.-Y. Li, and C.-C. Chen, "Single-antenna Doppler radars using self and mutual injection locking for vital sign detection with random body movement cancellation," *IEEE Trans. Microw. Theory Techn.*, vol. 59, no. 12, pp. 3577–3587, Dec. 2011.

[17] J. Tu, T. Hwang, and J. Lin, "Respiration rate measurement under 1-D body motion using single continuous-wave Doppler radar vital sign detection system," *IEEE Trans. Microw. Theory Techn.*, vol. 64, no. 6, pp. 1937–1946, Jun. 2016.

[18] Q. Lv, L. Chen, K. An, J. Wang, H. Li, D. Ye, J. Huangfu, C. Li, and L. Ran, "Doppler vital signs detection in the presence of large-scale random body movements," *IEEE Trans. Microw. Theory Techn.*, vol. 66, no. 9, pp. 4261–4270, Sep. 2018.

[19] A. Lazaro, D. Girbau, and R. Villarino, "Techniques for clutter suppression in the presence of body movements during the detection of respiratory activity through UWB radars," *Sensors*, vol. 14, no. 2, pp. 2595–2618, Feb. 2014.

[20] F. Khan and S. Cho, "A detailed algorithm for vital sign monitoring of a stationary/non-stationary human through IR-UWB radar," *Sensors*, vol. 17, no. 2, p. 290, Feb. 2017.

[21] S. Leem, F. Khan, and S. Cho, "Vital sign monitoring and mobile phone usage detection using IR-UWB radar for intended use in car crash prevention," *Sensors*, vol. 17, no. 6, p. 1240, May 2017.

[22] W. G. Carrara, R. M. Majewski, and R. S. Goodman, *Spotlight Synthetic Aperture Radar: Signal Processing Algorithms*. Boston, MA, USA: Artech House, 1995.

[23] U. Spagnolini, *Statistical Signal Processing in Engineering*. Hoboken, NJ, USA: Wiley, 2018.

[24] H. Munakata, S. Koshita, M. Abe, and M. Kawamata, "Improvement of convergence speed for an adaptive notch filter based on simplified lattice algorithm using pilot notch filters," in *Proc. IC-NIDC*, Sep. 2016, pp. 312–316.

[25] S. U. Pillai, *Array Signal Processing*. New York, NY, USA: Springer, 2012.

[26] J.-A. Ting, E. Theodorou, and S. Schaal, "A Kalman filter for robust outlier detection," in *Proc. IEEE/RSJ Int. Conf. Intell. Robots Syst.*, Oct. 2007, pp. 1514–1519.

[27] J.-A. Ting, E. Theodorou, and S. Schaal, "Learning an outlier-robust Kalman filter," in *Proc. ECML-PKDD*. Berlin, Germany: Springer, 2007, pp. 748–756.

[28] C. M. Bishop, *Pattern Recognition and Machine Learning*. New York, NY, USA: Springer, 2006.

[29] A. P. Dempster, N. M. Laird, and D. B. Rubin, "Maximum likelihood from incomplete data via the EM algorithm," *J. Roy. Stat. Soc., B, Methodol.*, vol. 39, no. 1, pp. 1–22, 1977.

[30] J. Tu and J. Lin, "Fast acquisition of heart rate in noncontact vital sign radar measurement using time-window-variation technique," *IEEE Trans. Instrum. Meas.*, vol. 65, no. 1, pp. 112–122, Jan. 2016.

[31] A. Francis, J. Sha-Ron, and U. Jeffrey, *Common Surgical Diseases*. 2020.

[32] C. Barfod, M. M. P. Lauritzen, J. K. Danker, G. Sölétormos, J. L. Forberg, P. A. Berlac, F. Lippert, L. H. Lundstrøm, K. Antonsen, and H. W. K. Lange, "Abnormal vital signs are strong predictors for intensive care unit admission and in-hospital mortality in adults triaged in the emergency department—A prospective cohort study," *Scand. J. Trauma, Resuscitation Emergency Med.*, vol. 20, no. 1, pp. 1–10, 2012.

[33] M. Li and J. Lin, "Wavelet-transform-based data-length-variation technique for fast heart rate detection using 5.8-GHz CW Doppler radar," *IEEE Trans. Microw. Theory Techn.*, vol. 66, no. 1, pp. 568–576, Jan. 2018.

[34] J. Saluja, J. Casanova, and J. Lin, "A supervised machine learning algorithm for heart-rate detection using Doppler motion-sensing radar," *IEEE J. Electromagn., RF Microw. Med. Biol.*, vol. 4, no. 1, pp. 45–51, Mar. 2020.

[35] M. B. Lotrič and A. Stefanovska, "Synchronization and modulation in the human cardiorespiratory system," *Phys. A, Stat. Mech. Appl.*, vol. 283, nos. 3–4, pp. 451–461, Aug. 2000.

[36] S. Perry, N. A. Khovanova, and I. A. Khovanov, "Control of heart rate through guided high-rate breathing," *Sci. Rep.*, vol. 9, no. 1, pp. 1–10, 2019.

ZHICHAO LAI (Graduate Student Member, IEEE) received the B.S. degree from the Harbin Engineering University, Harbin, China, in 2018. He is currently pursuing the master's degree with the Key Laboratory of Underwater Acoustic Signal Processing of Ministry of Education, Southeast University. His research interests include robust filter and radar signal processing.

DIANZE LI (Graduate Student Member, IEEE) received the B.S. degree from the Xidian University, Xi'an, China, in 2019. He is currently pursuing the master's degree with the Key Laboratory of Underwater Acoustic Signal Processing of Ministry of Education, Southeast University. His current research interests include areas of vital sign detection and radar signal processing.

QISONG WU (Member, IEEE) received the Ph.D. degree from Xidian University, Xi'an, China, in 2010. He was a Postdoctoral Associate with Duke University, Durham, NC, USA, from 2010 to 2013, and with Villanova University, Villanova, PA, USA, from 2013 to 2015. He is currently an Associate Professor with the Key Laboratory of Underwater Acoustic Signal Processing of Ministry of Education, Southeast University, Nanjing, China. His research interests include radar signal processing, sonar signal processing, array signal processing, sparse Bayesian learning, through-the-wall radar imaging, and synthetic aperture radar imaging.

ZENGYANG MEI received the B.S. degree from the Xidian University, Xi'an, China, in 2018. He is currently pursuing the master's degree with the Key Laboratory of Underwater Acoustic Signal Processing of Ministry of Education, Southeast University. His current research interests include areas of vital sign detection and radar signal processing.

DIXIAN ZHAO received the Ph.D. degree in electrical engineering from the University of Leuven (KU Leuven), Belgium, in 2015. He is currently a Full Professor with the National Mobile Communications Research Laboratory, Southeast University, Nanjing, China. His current research interests include millimeter-wave integrated circuits, transceivers, and phased-array systems for 5G, satellite, radar, and wireless power transfer applications. He serves as a Technical Program Committee (TPC) member or the sub-committee chair of several conferences, including the IEEE European Solid-State Circuits Conference (ESSCIRC), the IEEE Asian Solid-State Circuits Conference (A-SSCC), and the IEEE International Conference on Integrated Circuits, Technologies and Applications (ICTA).

• • •